Parity readout in Majorana box qubits from the dispersive to the resonant regime

Sara M. Benjadi and Reinhold Egger*
Institut für Theoretische Physik, Heinrich-Heine-Universität, 40225 Düsseldorf, Germany

(Received 6 March 2026; revised 10 June 2026; accepted 12 June 2026; published 6 July 2026)

We study theoretical models for charge reflectometry and capacitive readout of the Majorana parity degree of freedom in Majorana box qubits, considering decoherence channels within the framework of the Lindblad master equation. Noting that a parity-dependent dynamical susceptibility $\chi_z(\omega)$ governs both readout schemes, we provide a general expression for $\chi_z(\omega)$ which covers the full crossover from the resonant regime to the off-resonant dispersive regime. In addition, we reexamine previous results which were obtained under a semiclassical factorization assumption. Using three different error measures, we show that this approximation is quantitatively justified in the dispersive regime. In the resonant regime, however, we find deviations from exact reference data, obtained by numerical solution for the steady state of the full Lindblad equation. These deviations are typically of the order of a few percent in the considered error measures.

DOI: 10.1103/j2x7-1h9c

I. INTRODUCTION

Majorana bound states (MBSs) are predicted to exist in various platforms. Noting that a spatially separated pair of MBSs is equivalent to a single (nonlocal) fermion state, MBSs are of fundamental physical interest and could potentially be used as basic constituents in topological quantum information processing schemes. However, after initial enthusiasm [1], the clear-cut experimental identification of MBSs and, in particular, the operation of a Majorana qubit turned out to be a rather challenging endeavor. Many experiments were based on proximitized semiconductor nanowires realizing one-dimensional (1D) topological superconductors, where MBSs should be located at the ends of the wire. However, a number of alternative platforms, e.g., proximitized topological insulator devices [2,3], have also been studied. We refer to Refs. [4–7] for comprehensive reviews. More recently, the so-called topological gap protocol was employed for identifying parameter regions where devices are expected to harbor MBSs [8–10]. In addition, many aspects of Majorana physics can be emulated using a poor man's version of short Kitaev chains engineered by the fine-tuning of coupled quantum dots [11–15].

An intensely pursued topologically protected qubit candidate is defined by the Majorana box qubit (MBQ) [16], aka tetron [17]. For the MBQ, one considers a device harboring four MBSs under strong Coulomb blockade conditions such that the computational space associated with MBSs becomes equivalent to a qubit space [18–20]. The Coulomb charging energy then provides a natural protection against quasiparticle poisoning mechanisms and allows for unique functionalities of the resulting Majorana qubit. As a consequence, several theoretical proposals for scalable architectures relying on MBQs as basic elements have been put forward [17,21–25], see also Refs. [26–28] for related schemes. A key element in all these proposals is the practical availability of a reliable and fast readout scheme for measuring the parity of a MBS pair. Using the Majorana operators $\gamma_j = \gamma_j^\dagger$, with $\gamma_j^2 = 1$, where different Majorana operators anticommute, the parity operator for the Majorana pair γ_2 and γ_3 in Fig. 1 is $\hat{z} = i\gamma_2\gamma_3$, with eigenvalues $z = \pm 1$.

There are various options for performing a parity readout. Interferometric conductance and/or charge reflectometry parity readout schemes for MBQs have been suggested in Ref. [16], see also Refs. [29–32]. Parity readout can also be achieved by charge sensing of a quantum dot coupled to the MBS pair [33–40]. Recent parity readout experiments [9,15] were performed by measuring the quantum capacitance C_Q (which depends on z, as detailed below) in the dispersive regime, see also Refs. [17,41,42]. Motivated by the recent experimental progress [9,15], here, we provide a theoretical analysis of parity readout in a MBQ, also addressing the crossover from the dispersive to the resonant limit. Our results are basically agnostic to the choice of Majorana platform and may also be of interest for analyzing topologically trivial cases, where MBSs are effectively replaced by Andreev bound states [5]. In the context of capacitive parity readout in the dispersive limit, such aspects have recently been studied for noninteracting Majorana wires [42]. For concreteness, however, here, we focus on the ideal MBQ case. It is worth noting that the resonant (instead of the dispersive) regime can offer distinct advantages for MBQ parity readout [16].

The remainder of this paper is structured as follows. In Sec. II, we discuss two different MBQ parity readout schemes in some detail, namely, charge reflectometry and measurements of the quantum capacitance. In both cases, a parity-dependent dynamical susceptibility $\chi_z(\omega)$ encodes

*Contact author: reinhold.egger@uni-duesseldorf.de

Published by the American Physical Society under the terms of the Creative Commons Attribution 4.0 International license. Further distribution of this work must maintain attribution to the author(s) and the published article's title, journal citation, and DOI.

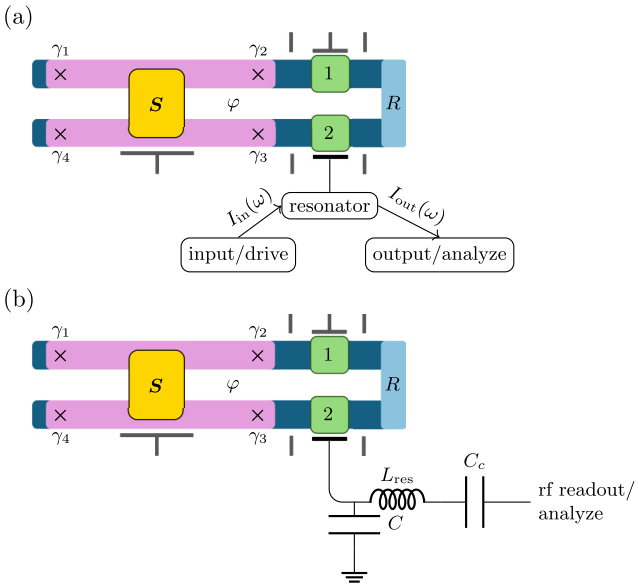


FIG. 1. Schematic readout schemes for the Majorana qubit parity $\hat{z} = i\gamma_2\gamma_3$, with eigenvalues $z = \pm 1$, see Eq. (1). The Majorana states $\gamma_{1,2,3,4}$ are boundary states of a pair of topological superconductor wires connected by a superconducting bridge (S) [16,17]. The floating Majorana box is operated under Coulomb valley conditions. A pair of small quantum dots (1 and 2, shown as green squares), with the double dot in the single-electron occupancy regime, is tunnel-coupled to the wire ends harboring γ_2 and γ_3, respectively. In addition to elastic cotunneling through the MBQ, coherent tunneling between dots 1 and 2 can proceed through a tunnel-coupled reference arm (R). The phase difference φ between both interfering tunneling paths can be tuned by gate voltages or by a weak perpendicular magnetic field. The fluctuating charge on dot 2 is monitored in the frequency domain by capacitively coupling dot 2 to a microwave cavity (photon resonator), which in turn is coupled to the readout circuit. (a) Charge reflectometry setup, where the outgoing intensity $I_{\rm out}(\omega)$ for given intensity $I_{\rm in}(\omega)$ in the input line is measured in a microwave circuit. (b) Quantum capacitance measurement, where the cavity is used for gate sensing and capacitance readout [9].

the parity sensitivity. To be specific, we separately study the resonant regime and the dispersive limit, where authors of previous work [16] have employed a semiclassical approximation to determine $\chi_z(\omega)$ from the Lindblad master equation. The latter equation governs the dynamics in the presence of decoherence channels. In Sec. III, we present a general expression for the susceptibility $\chi_z(\omega)$ which covers the entire crossover from resonant to off-resonant conditions. In addition, we examine the accuracy of the semiclassical approximation in both the strong-coupling (sc; resonant) limit and weak-coupling (wc; off-resonant dispersive) regime by comparing with exact reference results for experimentally realistic parameter choices. Here, reference results were either obtained by numerical solution for the steady state (ss) of the full Lindblad equation (in the sc regime) or follow from exact expressions (in the wc limit). Finally, Sec. IV contains concluding remarks. Throughout the paper, we use $\hbar = k_B = 1$.

II. MBQ PARITY READOUT SCHEMES

In this section, we discuss different MBQ parity readout schemes. After summarizing the setup and the theoretical model in Sec. II A, we describe two-port charge reflectometry readout in Sec. II B. The corresponding results in the resonant regime have already appeared in Ref. [16] (using the semiclassical approximation), but they are briefly reviewed here to keep the paper self-contained. In the dispersive limit, we obtain exact results beyond those in Ref. [16]. Next, in Sec. II C, we discuss MBQ parity readout via the quantum capacitance and show that the resonator susceptibility $\chi_z(\omega)$ appearing in the modeling of charge reflectometry readout also determines the capacitive readout scheme. Finally, in Sec. II D, we show that results for single-port charge reflectometry (used in Ref. [15]) can be directly inferred from the corresponding two-port results.

A. General remarks

A schematic setup for MBQ parity readout is shown in Fig. 1, where for concreteness, we assume a MBQ implementation in terms of two topological superconductor nanowires connected by a conventional superconductor bridge [16,17]. The entire superconducting island, which constitutes a topological variant of a Cooper pair box, is kept floating and is thus characterized by a finite charging energy E_C. For MBQs with lateral size of a few hundred nanometers, we estimate $E_C \sim 1$ meV. Operating the superconducting island near a Coulomb valley, the charging energy enforces a fermion parity constraint for energies $|E| \ll E_C$. Assuming broken time-reversal symmetry, the important low-energy MBQ degrees of freedom are the Majorana fermion operators $\gamma_1, \ldots, \gamma_4$ in Fig. 1, with the respective MBSs localized at the wire ends. The fermion parity constraint can then be expressed in terms of the total Majorana parity as, say, $\gamma_1\gamma_2\gamma_3\gamma_4 = +1$. The constrained Hilbert space of the island defines a nonlocal qubit with Pauli operators [16]

$$\hat{x} = i\gamma_1\gamma_2, \quad \hat{y} = i\gamma_3\gamma_1, \quad \hat{z} = i\gamma_2\gamma_3. \tag{1}$$

The spatial separation of the MBS pairs defining each Pauli operator provides a topological qubit protection mechanism [18–22]. We note that, for instance, disorder effects may cause topologically trivial low-energy Andreev bound state quasiparticles [5]. However, the approaches described below also allow for the readout of Andreev state parities, see also Refs. [9,42]. In what follows, we focus on the idealized case where only the γ_j values are kept as relevant degrees of freedom.

We study projective MBQ parity readout schemes for $z = \pm 1$, performed either by using charge reflectometry, see Fig. 1(a), or through a measurement of the quantum capacitance, see Fig. 1(b). However, by a modification of the setups in Fig. 1, also the parity operators $\hat{x}$ and $\hat{y}$ in Eq. (1) can be measured [16,17]. In Fig. 1, two quantum dots (1 and 2) are connected through tunnel barriers to the MBQ via γ_2 and γ_3, respectively. The double dot is operated in the coherent single-electron occupancy regime, such that only a single electron occupies the double dot on average. The corresponding dots are significantly smaller than the MBQ structure and therefore

come with an even higher charging energy than the MBQ, giving direct access to the single-electron occupancy regime for the double dot [16]. In addition to interdot cotunneling processes via the MBQ with effective tunneling amplitude $t_1\hat{z}$ [16,17], we include a direct reference arm with interdot tunneling amplitude t_0. The tunable phase φ in Fig. 1 refers to the relative phase difference between the complex amplitudes t_0 and t_1. The effective interdot tunneling amplitude due to the interference of both pathways is then given by

$$t_z = t_0 + t_1\hat{z}. \tag{2}$$

Note that the transmission probability $|t_z|^2$ depends on the MBQ parity $z = \pm$.

In the single-electron occupancy regime of the double dot, a basis for the Hilbert space of the double dot is given by localized states $\{|1\rangle_d, |2\rangle_d\}$, where we assume that only a single quantum level in each dot is energetically accessible. In this basis, the double dot in the presence of the tunneling amplitude t_z in Eq. (2) is described by the Hamiltonian

$$H_d = \begin{pmatrix} \varepsilon & t_z \\ t_z^* & -\varepsilon + \lambda\hat{Q}_s \end{pmatrix}, \tag{3}$$

where the bare level energies $\pm\varepsilon$ are due to the (gate-tunable) detuning ε, and the operator $\hat{Q}_s$ refers to a photon resonator (cavity) capacitively coupled to dot 2 with (weak) coupling strength λ. For $\lambda = 0$, the electron undergoes Rabi oscillations between both dots with the parity-dependent frequency

$$\omega_{z=\pm} = \sqrt{\varepsilon^2 + |t_0 + zt_1|^2}. \tag{4}$$

Transforming from $\{|1\rangle_d, |2\rangle_d\}$ to the Rabi eigenbasis for the Hilbert space of the double dot, we define Pauli operators $\tau_{x,y,z}$, with $\tau_\pm = (\tau_x \pm i\tau_y)/2$, with respect to the Rabi basis.

B. Charge reflectometry

Let us first address charge reflectometry readout [16,43–46], see Fig. 1(a), where a microwave resonator with photon creation operator $a^\dagger$ and bare frequency ω_0 is capacitively coupled to the charge on dot 2, with $\hat{Q}_s = a + a^\dagger$ in Eq. (3). For small coupling λ in Eq. (3), the Hamiltonian describing the resonator coupled to the double dot then takes the form [16]

$$H = \omega_z\tau_z + \omega_0 a^\dagger a + \frac{\lambda}{2}(a + a^\dagger)\left(1 - \frac{\varepsilon}{\omega_z}\tau_z - \frac{|t_z|}{\omega_z}\tau_x\right). \tag{5}$$

We now separately discuss the limiting cases of sc (near-resonant conditions) and wc (dispersive off-resonant conditions). We note that, in both limits, the coupling λ remains a small parameter.

1. Near-resonant conditions

First, if the resonator and the double dot are nearly resonant, $|\omega_0 - 2\omega_z| \ll \min(\omega_0, \omega_z)$ for both values of $z = \pm$, the standard rotating-wave approximation (RWA) applies [47]. As a result, Eq. (5) yields the effective Hamiltonian

$$H_{\rm RWA} = \omega_z\tau_z + \omega_0 a^\dagger a + g_z(a\tau_+ + a^\dagger\tau_-), \tag{6}$$

where the parity-dependent coupling

$$g_z = -\frac{\lambda|t_z|}{2\omega_z} \tag{7}$$

describes the absorption or emission of a resonator photon accompanying each interdot tunneling process. Below, the rates $\kappa_{\rm in,out}$ refer to photon leakage from the resonator into the microwave input or output lines, with the total leakage rate

$$\kappa = \kappa_{\rm in} + \kappa_{\rm out}. \tag{8}$$

Adding a single-tone input drive with frequency ω and intensity I_0 incident on the resonator

$$H_{\rm dr} = i\sqrt{\kappa_{\rm in} I_0}[e^{-i\omega t}a^\dagger - e^{i\omega t}a] \tag{9}$$

and transforming to the rotating frame of the drive, one arrives at the full sc Hamiltonian

$$H_{\rm sc} = \frac{\Delta_z}{2}\tau_z + \Delta_0 a^\dagger a + g_z(a\tau_+ + a^\dagger\tau_-) + i\sqrt{\kappa_{\rm in} I_0}(a^\dagger - a), \tag{10}$$

with the shifted dot and resonator frequencies

$$\Delta_z = 2\omega_z - \omega, \quad \Delta_0 = \omega_0 - \omega. \tag{11}$$

Considering dephasing and relaxation for the hybridized double dot as well as photon leakage effects within the standard Lindblad master equation approach [48], the dynamics of the density matrix $\rho(t)$ describing the coupled system defined by the double dot and the resonator obeys the Lindblad equation

$$\begin{aligned}\dot{\rho} = &-i[H_{\rm sc}, \rho] + \frac{\Gamma_\phi}{2}\mathcal{D}[\tau_z]\rho \\ &+\gamma\{(n_{\rm th}+1)\mathcal{D}[\tau_-]\rho + n_{\rm th}\mathcal{D}[\tau_+]\rho\} \\ &+\kappa\{(N_{\rm th}+1)\mathcal{D}[a]\rho + N_{\rm th}\mathcal{D}[a^\dagger]\rho\},\end{aligned} \tag{12}$$

where $\mathcal{D}[L]\rho = L\rho L^\dagger - \frac{1}{2}\{L^\dagger L, \rho\}$ is the Lindblad dissipator. The terms $\sim\kappa$ model photon leakage, and the rates Γ_ϕ and γ quantify dephasing and relaxation effects on the double dot, respectively. Assuming that a uniform temperature T is established by the environment, the thermal occupation factors in Eq. (12) are given by

$$n_{\rm th} = \frac{1}{e^{2\omega_z/T} - 1}, \quad N_{\rm th} = \frac{1}{e^{\omega_0/T} - 1}. \tag{13}$$

From Eq. (12), the expectation values $\langle a(t)\rangle = {\rm Tr}[a\rho(t)]$ and $\langle\tau_-(t)\rangle$ satisfy the coupled equations of motion

$$\begin{aligned}\langle\dot{a}\rangle &= -i\Delta_0\langle a\rangle - ig_z\langle\tau_-\rangle + \sqrt{\kappa_{\rm in} I_0} - \frac{\kappa}{2}\langle a\rangle, \\ \langle\dot{\tau}_-\rangle &= -i\Delta_z\langle\tau_-\rangle + ig_z\langle a\tau_z\rangle - \Gamma_{\rm tot}\langle\tau_-\rangle,\end{aligned} \tag{14}$$

with the total decay rate

$$\Gamma_{\rm tot} = \Gamma_\phi + \frac{\tilde{\gamma}}{2}, \quad \tilde{\gamma} = (2n_{\rm th}+1)\gamma. \tag{15}$$

However, due to the presence of $\langle a\tau_z\rangle$ in the equation for $\langle\dot{\tau}_-\rangle$, the equations in Eq. (14) couple to higher-order hierarchies of expectation values, and an exact solution appears to be out of reach.

To make approximate but analytical progress for the ss solutions of Eq. (14), reached at long times with $\langle\dot{a}\rangle_{\rm ss} = \langle\dot{\tau}_-\rangle_{\rm ss} = 0$, in Ref. [16], the authors have truncated the hierarchy by applying a semiclassical decoupling approximation

in Eq. (14)

$$\langle a\tau_z\rangle_{\rm ss} \approx \langle a\rangle_{\rm ss}\langle\tau_z\rangle_{\rm ss}, \tag{16}$$

where the decoherence effects in Eq. (12) imply

$$\langle\tau_z\rangle_{\rm ss} = -\tanh(\omega_z/T). \tag{17}$$

From Eqs. (14) and (16), the ss expectation values are then given by

$$\langle a\rangle_{\rm ss} = \frac{-i\sqrt{\kappa_{\rm in}I_0}}{-\frac{i}{2}\kappa + \Delta_0 - \chi_z\langle\tau_z\rangle_{\rm ss}},$$
$$\langle\tau_-\rangle_{\rm ss} = -\frac{\chi_z}{g_z}\langle a\rangle_{\rm ss}\langle\tau_z\rangle_{\rm ss}, \tag{18}$$

where the parity-dependent charge susceptibility is

$$\chi_z(\omega) = -\frac{g_z^2}{\Delta_z - i\Gamma_{\rm tot}}, \tag{19}$$

with g_z in Eq. (7) and Δ_z in Eq. (11). Under the approximation in Eq. (16), the ss transmission amplitude in the output line of Fig. 1(a) thus follows as [16]

$$A_\omega^{(\rm sc)} = \frac{\sqrt{\kappa_{\rm out}}\langle a\rangle_{\rm ss}}{\sqrt{I_0}} = \frac{-i\sqrt{\kappa_{\rm in}\kappa_{\rm out}}}{\Delta_0 - \frac{i}{2}\kappa - \chi_z\langle\tau_z\rangle_{\rm ss}}, \tag{20}$$

where sc emphasizes that this result applies to the sc limit. The susceptibility χ_z captures the parity-dependent reactive response arising from charge fluctuations, while A_ω characterizes the parity-dependent two-port response to a microwave drive. Parity readout of $\hat{z}$ is then possible either by tracking the peak in $|A_\omega|^2$ at the z-dependent frequency $\omega = \Omega_z$, where Ω_z follows from Eq. (20) by minimizing $|\omega_0 - \omega - \langle\tau_z\rangle_{\rm ss}{\rm Re}(\chi_z)|$, or by measuring the z-dependent phase shift $\delta\phi_z = -\arg(A_\omega)$ of the outgoing signal. The sc regime allows for fast high-contrast parity readout but requires sizable coupling λ and accurate experimental control over the tunable parameters of the device. Readout of the MBQ parity $z = \pm$ is thus possible by exploiting the z-dependence of χ_z.

It is one of the goals of the present work to check the accuracy of the semiclassical approximation in Eq. (16). We can thereby judge the accuracy of expressions like Eq. (20), which allow one to interpret experimental data for parity readout in the sc regime.

2. *Off-resonant conditions*

Next, we turn to the off-resonant case, realizing the dispersive regime of MBQ parity readout, see also Refs. [16,17,29,30]. Recent experimental readout schemes [9,15] have employed this regime. The dispersive regime is realized for $\lambda \ll \min(\omega_0, |\omega_0 \pm 2\omega_z|)$, so that only virtual photon processes are important. Expanding H in Eq. (5) up to second order in $\{\lambda/\omega_0, \lambda/\omega_z\}$, one finds the effective coupled dot-resonator Hamiltonian (up to a z-dependent constant) [16]

$$H_{\rm eff} = \left(\omega_z + \frac{\delta_z + \chi_z}{2}\right)\tau_z + (\omega_0 + \chi_z\tau_z)a^\dagger a, \tag{21}$$

where $\chi_z(\omega)$ now has the ω-independent (static) form

$$\chi_z = -\frac{g_z^2}{\omega_z - \omega_0^2/4\omega_z}. \tag{22}$$

We also use $\delta_z = \lambda^2\varepsilon/(\omega_0\omega_z)$. In analogy to Eq. (10), using $H_{\rm dr}$ in Eq. (9) and switching to the rotating frame of the drive, we arrive at the full wc Hamiltonian

$$H_{\rm wc} = \frac{\Delta_z + \delta_z + \chi_z}{2}\tau_z + (\Delta_0 + \chi_z\tau_z)a^\dagger a + i\sqrt{\kappa_{\rm in}I_0}(a^\dagger - a). \tag{23}$$

We again employ the Lindblad equation in Eq. (12) with $H_{\rm sc} \to H_{\rm wc}$ to include dephasing and relaxation effects on the double dot as well as photon leakage. Instead of Eq. (14), we arrive at the wc form of the equation of motion for $\langle a\rangle$

$$\langle\dot{a}\rangle = -i\Delta_0\langle a\rangle - i\chi_z\langle a\tau_z\rangle + \sqrt{\kappa_{\rm in}I_0} - \frac{\kappa}{2}\langle a\rangle. \tag{24}$$

Here, $\langle a\tau_z\rangle$ satisfies a closed equation of motion

$$\frac{d}{dt}\langle a\tau_z\rangle = -\left(i\Delta_0 + \frac{\kappa}{2} + \tilde{\gamma}\right)\langle a\tau_z\rangle - (i\chi_z + \gamma)\langle a\rangle + \sqrt{\kappa_{\rm in}I_0}\langle\tau_z\rangle, \tag{25}$$

with $\tilde{\gamma}$ in Eq. (15). If one again applies the semiclassical approximation in Eq. (16), the result for A_ω in the wc regime corresponding to dispersive (off-resonant) MBQ readout follows directly from Eq. (24)

$$A_\omega^{(\rm wc)} = \frac{-i\sqrt{\kappa_{\rm in}\kappa_{\rm out}}}{\Delta_0 - \frac{i}{2}\kappa + \chi_z\langle\tau_z\rangle_{\rm ss}}, \tag{26}$$

which formally coincides with the sc expression in Eq. (20) apart from a sign change in the χ_z term. Parity readout is again possible by determining χ_z from measurements of A_ω.

However, since Eq. (25) allows one to compute $\langle a\tau_z\rangle_{\rm ss}$ without further truncation, the exact form of $A_\omega = A_\omega^{(\rm wc,ex.)}$ can be determined analytically. With $\tilde{\gamma}$ in Eq. (15), we find

$$A_\omega^{(\rm wc,ex.)} = \frac{-i\sqrt{\kappa_{\rm in}\kappa_{\rm out}}\left[\Delta_0 - i\left(\frac{\kappa}{2} + \tilde{\gamma}\right) - \chi_z\langle\tau_z\rangle_{\rm ss}\right]}{\left(\Delta_0 - \frac{i}{2}\kappa\right)\left[\Delta_0 - i\left(\frac{\kappa}{2} + \tilde{\gamma}\right)\right] - (\chi_z - i\gamma)\chi_z}. \tag{27}$$

From this expression, one recovers the approximate result in Eq. (26) (obtained under the semiclassical approximation) as follows. We first assume that relaxation effects on the double dot are subleading, such that terms $\propto\gamma, \tilde{\gamma}$ in Eq. (27) can be neglected. Using $|\chi_z\langle\tau_z\rangle_{\rm ss}| \ll |\Delta_0 - i\frac{\kappa}{2}|$, which is expected to hold in the wc regime, see Eq. (22), we may write $1 - \frac{\chi_z\langle\tau_z\rangle_{\rm ss}}{\Delta_0 - i\frac{\kappa}{2}} \simeq (1 + \frac{\chi_z\langle\tau_z\rangle_{\rm ss}}{\Delta_0 - i\frac{\kappa}{2}})^{-1}$. In addition, we neglect the term $\propto (\chi_z - i\gamma)\chi_z$ in the denominator of Eq. (27) in view of the smallness of χ_z. With these approximations, Eq. (27) reduces to Eq. (26). We conclude that the approximation in Eq. (16) is justified for very weak relaxation effects on the dot and for very small susceptibility χ_z. For a more detailed comparison of Eqs. (26) and (27), see Sec. III B.

C. Quantum capacitance

We now turn to the setup in Fig. 1(b), where MBQ parity readout is performed by measuring the z-dependent quantum capacitance $C_{Q;z}$. If the tunneling amplitude t_0 through the reference arm is much bigger than the cotunneling amplitude t_1, the two quantum dots are effectively hybridized to form a single dot which is tunnel-coupled to both Majorana operators γ_2 and γ_3. The energy shift of this dot then depends on $\hat{z}$ which can be read out by measuring $C_{Q;z}$. Interestingly, our results obtained for the susceptibility χ_z, which determines the

charge reflectometry parity readout scheme in Sec. II B, can be translated into results for the effective parity-dependent quantum capacitance $C_{Q;z}$. Similarly, the two-port transmission amplitude A_ω can be recast as one-port reflection coefficient S_{11}^M, corresponding to the measured signal in the one-port reflectometry setup in Ref. [15], see Sec. II D.

The Hamiltonian in Eq. (5) describes the double dot coupled to the resonator in the presence of the parity-dependent hopping amplitude t_z in both wc and sc regimes, including the crossover between both limits. Here, the MBQ parity is contained in the term $H_I = g_z(a + a^\dagger)\tau_x$. For the quantum capacitance readout sketched in Fig. 1(b), the corresponding form of H_I, denoted by $\tilde{H}_I$ below, is obtained by transforming the capactive coupling between the resonator and dot 2 into the Rabi basis of the double dot. We then find

$$\tilde{H}_I = -\alpha e\sqrt{\frac{\omega_0}{2C_z}}(a + a^\dagger)\tau_x, \tag{28}$$

where C_z is the total effective capacitance of the readout circuit, which includes the resonator capacitance C_r and the quantum capacitance $C_{Q;z}$. The quantity α in Eq. (28) is a lever arm [9]. By comparing H_I and $\tilde{H}_I$, we obtain the correspondence

$$g_z = -\alpha e\sqrt{\frac{\omega_0}{2C_z}}. \tag{29}$$

We now consider the linear-response regime, where the induced charge on dot 2 is connected to the applied drive voltage $V(\omega)$ through the charge susceptibility $\tilde{\chi}_z(\omega)$ of the double dot. Following the unified framework of Ref. [49], the admittance is then given by

$$Y(\omega) = -i\omega(\alpha e)^2\tilde{\chi}_z, \tag{30}$$

which identifies the reactive part of the response $Y(\omega) = i\omega C_{Q;z}$, as an effective z-dependent quantum capacitance

$$C_{Q;z} = -(\alpha e)^2\tilde{\chi}_z. \tag{31}$$

In the device circuitry of Fig. 1(b), the reactive response due to the double dot provides a small parity-dependent quantum capacitance contribution $C_{Q;z}$ in parallel with the resonator capacitance C_r. We note that the resonator susceptibility χ_z is related to the susceptibility of the double dot by the relation $\chi_z = g_z^2\tilde{\chi}_z$. With $C_{Q;z} \ll C_r$, from Eq. (31), we arrive at the relation, see also Ref. [9],

$$C_{Q;z}(\omega) = -\frac{2C_r}{\omega_0}\chi_z(\omega). \tag{32}$$

The minus sign implies that a positive reactive susceptibility [$\mathrm{Re}(\chi_z) > 0$] corresponds to a reduction of the effective quantum capacitance, implying an upward shift of the resonator frequency. By virtue of Eq. (32), results for the charge reflectometry setup are directly connected to quantum capacitance readout protocols. In both approaches, χ_z is the central z-dependent quantity of interest.

D. Single-port reflectometry

Here, we briefly show that the parity-dependent single-port reflectometry signal S_{11}^M measured in Ref. [15] is also equivalent to the knowledge of A_ω. We start from the standard input-output description of a resonator connected to two ports as in Fig. 1(a), where the cavity field $a(\omega)$ in frequency space is connected to the incoming and outgoing fields $b_{\mathrm{in,out}}(\omega)$ and $c_{\mathrm{in,out}}(\omega)$ in the two ports through the relations [50]

$$\begin{aligned} a(\omega) &= \mathcal{R}(\omega)[\sqrt{\kappa_{\mathrm{in}}}b_{\mathrm{in}}(\omega) + \sqrt{\kappa_{\mathrm{out}}}c_{\mathrm{in}}(\omega)], \\ b_{\mathrm{out}}(\omega) &= b_{\mathrm{in}}(\omega) - \sqrt{\kappa_{\mathrm{in}}}a(\omega), \\ c_{\mathrm{out}}(\omega) &= c_{\mathrm{in}}(\omega) - \sqrt{\kappa_{\mathrm{out}}}a(\omega). \end{aligned} \tag{33}$$

The complex function $\mathcal{R}(\omega)$ characterizes the internal resonator response and contains the parity-dependent signal. In this two-port configuration, the drive is applied at the input port, i.e., $c_{\mathrm{in}} = 0$. The transmitted amplitude in the output port is then given by

$$S_{21}(\omega) = \frac{\langle c_{\mathrm{out}}(\omega)\rangle}{\langle b_{\mathrm{in}}(\omega)\rangle} = -\sqrt{\kappa_{\mathrm{in}}\kappa_{\mathrm{out}}}\mathcal{R}(\omega). \tag{34}$$

For drive amplitude $\langle b_{\mathrm{in}}(\omega)\rangle = \sqrt{I_0}$, the ss cavity field is then given by $\langle a(\omega)\rangle_{\mathrm{ss}} = \sqrt{\kappa_{\mathrm{in}}I_0}\mathcal{R}(\omega)$, and we arrive at

$$A_\omega = \sqrt{\frac{\kappa_{\mathrm{out}}}{I_0}}\langle a(\omega)\rangle_{\mathrm{ss}} = S_{21}(\omega). \tag{35}$$

Similarly, for a single-port configuration, the reflected amplitude at the port follows as

$$S_{11}(\omega) = \frac{\langle b_{\mathrm{out}}(\omega)\rangle}{\langle b_{\mathrm{in}}(\omega)\rangle} = 1 - \kappa_{\mathrm{in}}\mathcal{R}(\omega). \tag{36}$$

Using Eqs. (34) and (36), we arrive at the general relation

$$S_{11}(\omega) = 1 + \sqrt{\frac{\kappa_{\mathrm{in}}}{\kappa_{\mathrm{out}}}}S_{21}(\omega) = 1 + \sqrt{\frac{\kappa_{\mathrm{in}}}{\kappa_{\mathrm{out}}}}A_\omega. \tag{37}$$

We emphasize that $S_{11} = S_{11}^M$ again contains the parity-dependent reflectometry signal. This readout scheme was used in Ref. [15].

III. RESULTS

In this section, we first derive an expression for the susceptibility χ_z valid in the full crossover regime from wc to sc, see Sec. III A. This expression is of particular interest for quantum capacitance readout. We compare it to the corresponding approximate expressions valid in the wc and sc limits, see Eqs. (22) and (19), respectively, to estimate their accuracy in different parameter regimes. In Sec. III B, we then turn to an assessment of the accuracy of expressions based on the semiclassical approximation in Eq. (16), which has been employed for deriving the charge reflectometry amplitude A_ω in Sec. II. Specifically, we compare the sc and wc expressions for A_ω in Eqs. (20) and (26) to exact results. In the sc limit, the exact ss is obtained by numerical simulation of the full Lindblad equation in Eq. (12). In the wc limit, we instead compare with the exact result for A_ω in Eq. (27).

A. Susceptibility for the full crossover

We start by computing the dynamical susceptibility associated with the cavity-qubit coupling operator in Eq. (5) for the entire crossover from wc to sc. From the linear coupling term

$(a + a^\dagger)\hat{D}$ in Eq. (5), we identify the operator

$$\hat{D} = \frac{\lambda}{2}\left(1 - \frac{\varepsilon}{\omega_z}\tau_z - \frac{|t_z|}{\omega_z}\tau_x\right). \tag{38}$$

We consider this coupling as weak perturbation and treat it by linear response theory. The susceptibility thus follows from a Kubo formula [51]

$$\chi_z^{\rm full}(t) = -i\,\Theta(t)\,\langle[\hat{D}(t), \hat{D}(0)]\rangle_0, \tag{39}$$

where the average is taken with respect to the $\lambda = 0$ problem. Since $[\tau_z(t), \tau_z(0)] = 0$ in the absence of the coupling, only the term $\propto\tau_x$ in Eq. (38) contributes to Eq. (39). We can therefore effectively replace $\hat{D} \to g_z\tau_x$ with g_z in Eq. (7) when computing $\chi_z^{\rm full}(t)$. The correlator in Eq. (39) can be analytically evaluated, considering dephasing and decoherence processes in the Lindblad equation in Eq. (12) via the rate $\Gamma_{\rm tot}$ in Eq. (15). After a Fourier transform, we find

$$\chi_z^{\rm full}(\omega) = g_z^2\left[\frac{1}{i\Gamma_{\rm tot} - (2\omega_z - \omega)} - \frac{1}{i\Gamma_{\rm tot} + (2\omega_z + \omega)}\right]. \tag{40}$$

This expression describes the susceptibility for the full crossover from wc to sc within linear-response theory, i.e., considering terms up to the order g_z^2. The first term in Eq. (40) corresponds to the resonant contribution near $\omega \simeq 2\omega_z$, which is kept within RWA for the sc case, while the second term represents the counterrotating contribution. In the near-resonant limit $\omega \approx 2\omega_z$, the off-resonant second term can be neglected, leading to the susceptibility expression in Eq. (19) for the sc limit. Conversely, setting $\omega \approx \omega_0$ in Eq. (40) and expanding both denominators for large detuning $|\omega_0 \pm 2\omega_z| \gg \max\{|g_z|, \Gamma_{\rm tot}\}$, we recover the leading-order static dispersive pull in the wc regime, see Eq. (22).

To quantify the validity range of the approximate susceptibility expressions in Eqs. (19) and (22), let us compare them with the full susceptibility in Eq. (40) in more detail. We quantify the accuracy of each approximation by evaluating the relative deviation

$$\varepsilon = \frac{\left|\chi_z^{\rm full} - \chi_z^{\rm appr}\right|}{\left|\chi_z^{\rm full}\right|}, \tag{41}$$

computed separately for the sc limit, with $\chi_z^{\rm appr}$ in Eq. (19), and for the dispersive limit, see Eq. (22). Keeping the z dependence implicit, i.e., writing the coupling strength as $g = g_z$, and for simplicity setting $\omega = \omega_0$, the detuning is quantified by the dimensionless parameter

$$\varrho = \frac{\omega_0 - 2\omega_z}{g}, \tag{42}$$

where $|\varrho| \ll 1$ corresponds to the resonant regime, and $|\varrho| \gg 1$ characterizes the wc limit. Figure 2 tests the accuracy of Eqs. (19) and (22), which apply in the sc and wc regimes, respectively, across the full crossover as function of ϱ. Typical experimental values for ω_0 and ω_z are in the gigahertz regime. The decoherence rate $\Gamma_{\rm tot}$ and the coupling strength g are taken in the megahertz range. Those values are consistent with MBQ proposals and recent experiments on InAs-Al hybrid devices [9,16,26].

In Fig. 2(a), the coupling strength g is varied for a fixed value of $\Gamma_{\rm tot}$. Close to resonance ($\varrho \simeq 0$), the sc limit is (as expected) accurately captured by Eq. (19) since the counterrotating contribution in Eq. (40) is far off resonance. At the same time, the dispersive result in Eq. (22) breaks down. As ϱ increases, the wc expression in Eq. (22) becomes progressively more accurate, while the sc result in Eq. (19) becomes increasingly less accurate. Decreasing the coupling strength g broadens the interval in ϱ over which neither approximation is accurate, indicating that the width of the crossover region depends on g. For instance, for $g = 10$ MHz, the error ε exceeds an error threshold of 2% for both approximations within the detuning window $10 \lesssim \varrho \lesssim 50$, while for $g = 40$ MHz, this window shrinks to $2 \lesssim \varrho \lesssim 12$.

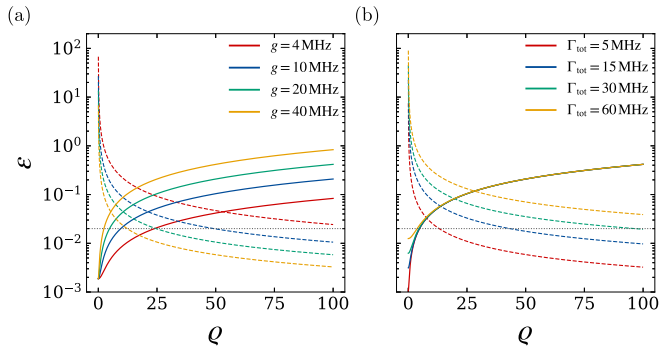


FIG. 2. Relative deviation ε in Eq. (41) vs normalized detuning ϱ in Eq. (42), comparing the full susceptibility expression in Eq. (40) with approximate expressions. Note the logarithmic scales for ε. Here, ϱ is changed by ramping up $\omega_0 - 2\omega_z$ at given coupling strength g. Since $\varepsilon(-\varrho) \simeq \varepsilon(\varrho)$, we depict only $\varepsilon(\varrho \geqslant 0)$. Solid curves show ε using the sc approximation for χ_z in Eq. (19), and dashed curves refer to the wc approximation in Eq. (22). The horizontal dotted line indicates a 2% error threshold. (a) ε vs ϱ for several values of g in the range 4 MHz $\leqslant g \leqslant$ 40 MHz with fixed total decoherence rate $\Gamma_{\rm tot} = 9$ MHz. (b) Same as (a) but for several values of $\Gamma_{\rm tot}$ in the range 9 MHz $\leqslant \Gamma_{\rm tot} \leqslant$ 60 MHz with fixed coupling strength $g = 20$ MHz.

Next, Fig. 2(b) illustrates the effect of the decoherence rate $\Gamma_{\rm tot}$ at fixed coupling. Increasing $\Gamma_{\rm tot}$ broadens the resonance in Eq. (40), thereby softening the breakdown of the wc result for small ϱ and generally increasing the error level for both approximations. Strong decoherence rates smoothen out the resonant structure and tend to invalidate both approximations. For MBQ parity readout, one thus must work with small $\Gamma_{\rm tot}$.

To summarize, Fig. 2 shows that Eq. (40) reproduces the expected behavior in both limits. In the near-resonant regime, it reduces to the sc susceptibility in Eq. (19), while for large detuning, it approaches the wc result in Eq. (22). The full susceptibility expression in Eq. (40) provides a consistent description across the full parameter range.

B. Tests of the semiclassical approximation

Next, we turn to tests of the validity of the semiclassical approximation in Eq. (16). To do so, we compare the approximate ss predictions in Sec. II B to exact reference values. In the sc limit, these are obtained from a numerical solution for the ss of the Lindblad equation in Eq. (12), retaining the full coupled photon-qubit dynamics. In the wc limit, we instead use the exact results discussed in Sec. II B. The comparison

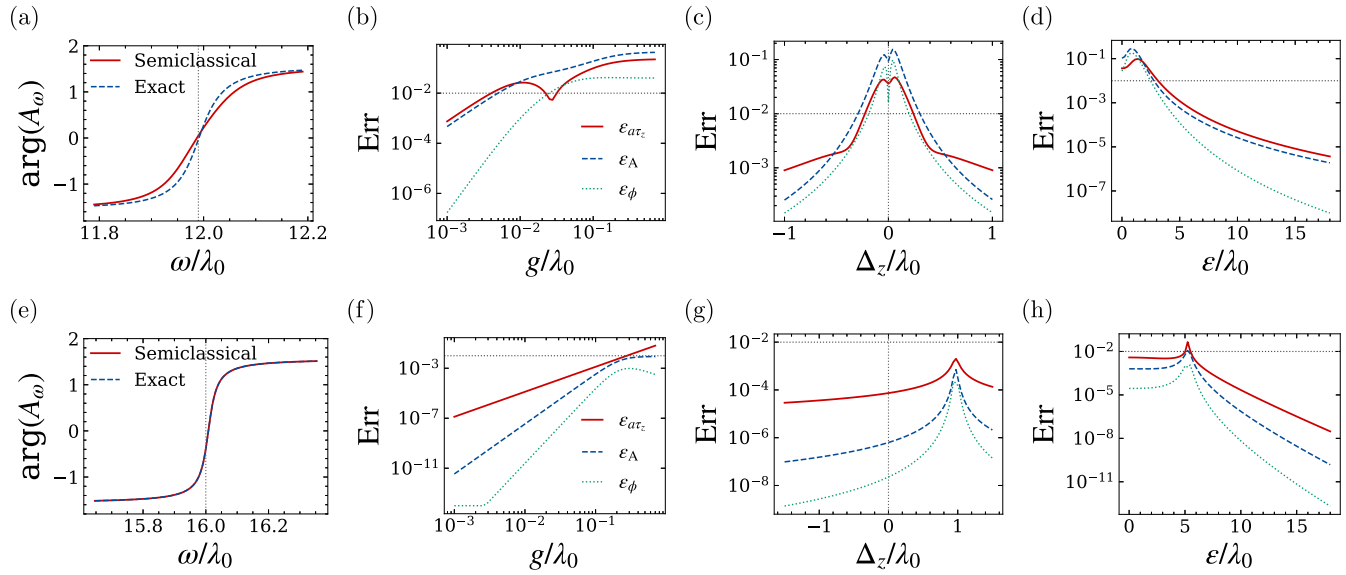


FIG. 3. Comparison of semiclassical and exact results in the sc and wc limits. We use the dimensionless numbers $\{\varepsilon_{a\tau_z}, \varepsilon_A, \varepsilon_\phi\}$ in Eqs. (43)–(45), which are shown on logarithmic scales. Employing the scale $\lambda_0 = 0.2$ GHz, we assume the tunnel couplings $|t_0| = 5\lambda_0$ and $|t_1| = \lambda_0$. For $z = +1$ and $\varphi = 0$, we have $|t_z| = |t_0 + t_1| = 6\lambda_0$. The cavity linewidth is $\kappa = 0.04\lambda_0$. Results are shown at temperature $T = 30$ mK. (a)–(d) sc limit. Unless noted otherwise, we choose the quantum-dot detuning $\varepsilon = 0$, see Eq. (3), with ω_z resulting from Eq. (4), the bare cavity frequency $\omega_0 = 11.99\lambda_0$, the rates $\gamma = 0.003\lambda_0$ and $\Gamma_\phi = 0.1\lambda_0$, the drive frequency $\omega = \omega_0$, and the cavity-dot coupling $\lambda = 0.1\lambda_0$, with g obtained from Eq. (7). Panel (a) shows the phase of A_ω vs ω. The dotted vertical line indicates the resonance at $\omega = \omega_0$. Panels (b)–(d) show the error measures as a function of g, of the detuning $\Delta_z = 2\omega_z - \omega$, and of ε, respectively. Dotted horizontal lines mark an error level of 1%. (e)–(h) Same as (a)–(d) but for the wc limit. Unless noted otherwise, here, we use $\varepsilon = 6\lambda_0$, $\lambda = 0.25\lambda_0$, $\gamma = 0.015\lambda_0$, $\Gamma_\phi = 0.05\lambda_0$, $\omega_0 = 16\lambda_0$, and $\omega = \omega_0$. In that case, $|\omega_0 - 2\omega_z| \sim O(\lambda)$.

is performed both for photon-qubit operator correlations encoded by $\langle a\tau_z\rangle_{\rm ss}$ and for the complex transmission amplitude A_ω used for MBQ parity readout in charge reflectometry.

First, we recall that the semiclassical approximation in Eq. (16) assumes $\langle a\tau_z\rangle_{\rm ss} \approx \langle a\rangle_{\rm ss}\langle\tau_z\rangle_{\rm ss}$, thus neglecting connected photon-qubit correlations. As dimensionless measure for the quality of this approximation, we study the normalized connected correlator

$$\varepsilon_{a\tau_z} = \frac{|\langle a\tau_z\rangle_{\rm s} - \langle a\rangle_{\rm ss}\langle\tau_z\rangle_{\rm ss}|}{|\langle a\rangle_{\rm ss}|}, \tag{43}$$

which probes the importance of correlations discarded in the approximation. (One could alternatively use $|\langle a\rangle_{\rm ss}\langle\tau_z\rangle_{\rm ss}|$ in the denominator, but for the parameter regimes considered below, this makes no significant difference.) Large values of $\varepsilon_{a\tau_z}$ indicate a breakdown of the semiclassical approximation. Second, to assess the impact of photon-qubit correlations on measurable quantities, we define a bounded symmetric relative error for A_ω

$$\varepsilon_{\rm A} = \frac{|A_{\rm semicl} - A_{\rm ref}|}{|A_{\rm semicl}| + |A_{\rm ref}|}, \tag{44}$$

where $A_{\rm semicl}$ is the semiclassical (approximate) result and $A_{\rm ref}$ the exact reference solution. In addition, since the phase of A_ω often provides the most sensitive signature in parity readout experiments, we also consider the normalized phase deviation

$$\varepsilon_\phi = \frac{|\arg(A_{\rm semicl}) - \arg(A_{\rm ref})|}{\pi}. \tag{45}$$

The combined set $\{\varepsilon_{a\tau_z}, \varepsilon_{\rm A}, \varepsilon_\phi\}$ allows us to distinguish between small quantitative deviations in the readout signal and a genuine breakdown of the semiclassical approximation in different parameter regimes. We perform the comparison for parameters that are realistic for hybrid Majorana devices such as those studied in Refs. [8,9,15].

1. Strong-coupling limit

In the sc limit, the three error measures introduced above are evaluated by comparing the semiclassical predictions in Sec. II B with the numerically exact solution for the ss of the Lindblad equation. Our results are shown in Figs. 3(a)–3(d) for a specific parameter set, where the system is in the sc regime such that coherent exchange dominates over dissipative broadening [47]. Figure 3(a) compares semiclassical and exact results for the transmission phase $\arg(A_\omega)$ as a function of the drive frequency ω. The semiclassical approximation captures the characteristic phase rotation, but close to resonance $\omega \simeq \omega_0$, quantitative deviations are visible. The slope of the phase response differs, indicating that coherent photon-qubit hybridization effects modify the dynamical response beyond semiclassics. Nonetheless, the deviations remain of moderate size. The phase error ε_ϕ remains below 10% across the shown frequency range.

A systematic comparison between the semiclassical and exact solutions is provided in Figs. 3(b)–3(d), where we show the dependence of the three error measures [see Eqs. (43)–(45)] on the coupling strength g, on the qubit-drive detuning Δ_z in Eq. (11), and on the double-dot detuning ε in Eq. (3),

respectively. Figure 3(b) shows that, for small g, all error measures grow with increasing g, indicating the growing importance of coherent mixing and correlation effects. Interestingly, $\varepsilon_{a\tau_z}$ exhibits a minimum at an intermediate value of g. This dip signals a crossover regime, where dissipative broadening suppresses the buildup of photon-qubit correlations while coherent hybridization does not yet dominate. However, in view of Eq. (43), this minimum can also be partially influenced by the fact that $|\langle a\rangle_{\rm ss}|$ varies with g. For larger values $g \gtrsim (\kappa, \gamma)$, hybridization effects dominate, and all error measures grow with increasing g. For the entire parameter range in Fig. 3(b), all error measures remain below the 10% margin.

Next, in Fig. 3(c), we show the dependence of the error measures on the detuning $\Delta_z = 2\omega_z - \omega$. All error measures exhibit maxima near $\Delta_z = 0$, where coherent exchange between photons and the double dot becomes most efficient, leading to maximal values of the connected photon-qubit correlations $|\langle a\tau_z\rangle_{\rm ss} - \langle a\rangle_{\rm ss}\langle\tau_z\rangle_{\rm ss}|$ and, consequently, to shortcomings of Eq. (16). We note that a small antidip is visible in the error measures at $\Delta_z = 0$. This feature can be rationalized by noting that χ_z becomes purely imaginary for $\Delta_z = 0$, i.e., the double dot causes only additional damping but no frequency shift of the cavity. The semiclassical approximation is then slightly better, resulting in a smaller error. We note that even close to the peaks centered near $\Delta_z = 0$, all three errors remain again below the 10% level. With increasing $|\Delta_z|$, they rapidly drop below 1%.

Finally, Fig. 3(d) shows the dependence on the scale ε, which enters the Rabi frequency ω_z in Eq. (4). Since the results for $\varepsilon \to -\varepsilon$ are identical, we consider only $\varepsilon \geqslant 0$ in Fig. 3(d). For small ε, where the effective qubit splitting is minimal and hybridization effects are strongest, all error measures reach their maximal values. Increasing ε enhances the energy separation between the qubit and the cavity, thereby suppressing coherent exchange processes. Correspondingly, all error measures decrease rapidly with increasing ε.

For the considered parameter values, the errors therefore always remain in the few-percent range, never exceeding the 10% level. While the semiclassical approximation is not exact, it remains rather accurate, and the corresponding expressions can be used for interpreting MBQ parity readout experiments unless one works in a low-contrast regime where $z = \pm 1$ outcomes are hard to distinguish. In such cases, one should employ a numerical solution of the full Lindblad equation to compare experimental data with theoretical predictions. We emphasize that deviations from semiclassical estimates become larger near resonance and/or for large coupling strengths.

2. *Weak-coupling regime*

We now turn to the dispersive wc regime, see Figs. 3(e)–3(h), where the cavity and the double dot are energetically detuned and coherent hybridization effects are suppressed. In contrast with the sc limit, the semiclassical approximation can now be benchmarked against analytical expressions, see Sec. II B. We again assess the accuracy of the approximation by means of the error measures $\{\varepsilon_{a\tau_z}, \varepsilon_{\rm A}, \varepsilon_\phi\}$. For the parameters in Figs. 3(e)–3(h), we have $g \ll |\omega_0 - 2\omega_z|$ and $g \lesssim (\kappa, \gamma)$. In this wc regime, the semiclassical approach effectively corresponds to retaining the leading dispersive frequency shift induced by the double dot on the cavity, while higher-order dynamical corrections are suppressed [32,47].

In Fig. 3(e), both the approximate and exact results for $\arg(A_\omega)$ are shown as a function of the drive frequency ω. In contrast with the sc limit in Fig. 3(a), the phase response is reproduced almost perfectly by the semiclassical approximation, with no visible discrepancy in slope or magnitude. In the dispersive limit, the qubit remains close to its equilibrium state, and photon-qubit correlations are strongly suppressed. As a result, the semiclassical decoupling provides an accurate description of both amplitude and phase.

The error measures are studied in Figs. 3(f)–3(h). First, in Fig. 3(f), we study their dependence on the coupling strength g. All three error measures increase monotonically with the effective coupling strength g. A significant error $\varepsilon_{a\tau_z}$ is visible at wc already, while the amplitude error ε_A and the phase error ε_ϕ remain extremely small for $g \lesssim 0.1\lambda_0$ and only approach the 1% threshold for $g \gtrsim 0.2\lambda_0$. This reflects the fact that the dispersive shift $\chi_z \propto g^2$ sets the scale of the cavity pull. Increasing g enhances the static frequency shift and increases qubit-cavity correlations not captured by the semiclassical factorization. Because the leading-order dispersive susceptibility is real and frequency independent, no resonant enhancement occurs, and all error measures grow monotonically with g. Nonetheless, for almost the full parameter range in Fig. 3(f), the three error measures, including $\varepsilon_{a\tau_z}$, remain below 1%.

In Fig. 3(g), we show the dependence on the detuning Δ_z. In contrast with the sc regime, no pronounced resonance peak occurs near $\Delta_z = 0$. Instead, all error measures remain orders of magnitude below the 1% level for the entire range shown. A smooth maximum is observed around $\Delta_z \simeq \lambda_0$, where the effective detuning between the cavity and the qubit transition becomes minimal within the scanned interval. At this point, the energy denominator entering the dispersive susceptibility is smallest, such that higher-order dynamical corrections beyond the leading dispersive approximation become pronounced. However, even near this maximum, the connected correlator $\varepsilon_{a\tau_z}$ and the amplitude error $\varepsilon_{\rm A}$ remain at or below the 0.1% level, with even smaller phase errors ε_ϕ.

Similarly, in Fig. 3(h), the dependence on ε reveals a pronounced maximum in the error measures around $\varepsilon \simeq 5\lambda_0$. At this point, the qubit splitting $2\omega_z$ is closest to the cavity frequency within the scanned interval, thereby minimizing the effective detuning $|\omega_0 - 2\omega_z|$. For larger ε, the qubit splitting grows, and the cavity-qubit detuning increases again. The dispersive condition is therefore reinforced, leading to rapid suppression of all error measures. Both the connected correlator $\varepsilon_{a\tau_z}$ and the amplitude error $\varepsilon_{\rm A}$ decrease by several orders of magnitude as ε increases. Even at the maximum near $\varepsilon \simeq 5\lambda_0$, however, the deviations remain at or below 1%.

In addition, in Fig. 4, we analyze the dependence of the error measures on the relaxation rate γ to test the approximation made in deriving the semiclassical expression from Eq. (27), where terms proportional to γ were dropped. In the wc regime considered in Fig. 4, all error measures remain well below 1%. For increasing γ, we find that $\varepsilon_{a\tau_z}$ and $\varepsilon_{\rm A}$ decrease

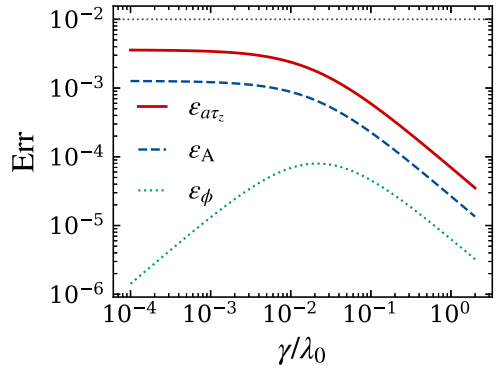


FIG. 4. Dependence of the error measures $\varepsilon_{a\tau_z}$, ε_A, and ε_ϕ on the relaxation rate γ of the double dot in the wc limit. Semiclassical results are compared with the exact analytical expressions in Sec. II B, see Eq. (27). The dashed horizontal line indicates the 1% level. All energies are expressed in units of $\lambda_0 = 0.2$ GHz.

monotonically. One can rationalize this finding by noting that strong relaxation broadens the double-dot transition and thereby suppresses coherent exchange processes between the cavity and the double dot. This effect reduces dynamical corrections beyond the leading dispersive approximation. The weak dependence of the phase error also confirms that the neglect of γ in the derivation of Eq. (26) from Eq. (27) is justified for typical experimentally relevant parameters in the dispersive regime.

3. *Finite-temperature effects*

We finally turn to the impact of thermal effects on MBQ parity readout and the accuracy of the corresponding semiclassical expressions. To study this question, we have performed additional simulations at elevated temperatures, see Fig. 5. Throughout this analysis, all parameters were kept fixed at the values used in Fig. 3, while temperature has been varied. Figure 5(a) shows the temperature dependence of the three error measures introduced in Eqs. (43)–(45) in the sc regime. At low temperatures, all these error measures approach constant values, indicating that, here, the dominant source for deviations from the semiclassical expression is not of thermal origin but rather due to the intrinsic breakdown of the semiclassical approximation caused by coherent photon-qubit correlations. As temperature increases, the connected-correlator error $\varepsilon_{a\tau_z}$ develops a broad maximum around $T \simeq 0.1$K. This behavior arises from the thermal occupation of the excited double-dot state, which enhances photon-qubit correlations and thereby increases the deviations from the semiclassical approximation. Interestingly, the amplitude error ε_A remains close to the 10% level throughout the considered temperature range, indicating that the parity-dependent cavity response remains sensitive to correlation effects. At even higher temperatures, all three error measures decrease again due to the thermal averaging of the double-dot state. Indeed, as $\langle\tau_z\rangle_{ss} \to 0$, the parity-dependent cavity response is progressively reduced, leading to a suppression of coherent photon-qubit correlations.

The corresponding results in the wc limit are shown in Fig. 5(b). In contrast with the sc case, all error measures are

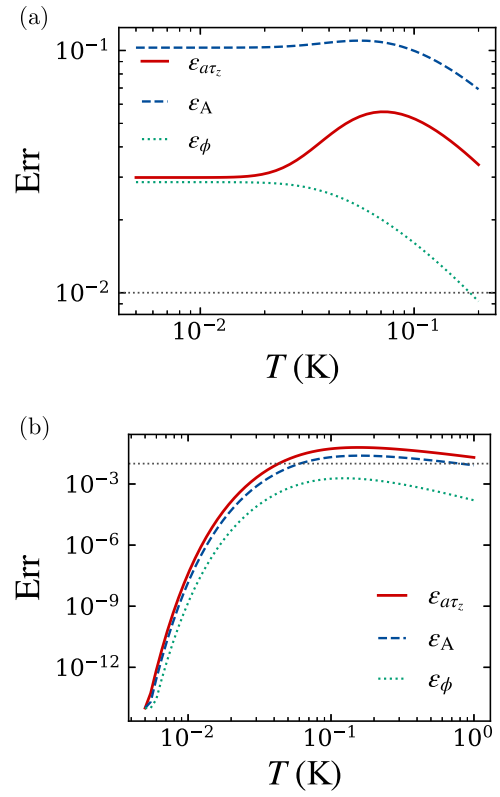


FIG. 5. Impact of thermal effects on different error measures for MBQ parity readout. Apart from temperature, the same model parameters as in Fig. 3 have been taken. The dotted horizontal line indicates an error threshold of 1%. (a) sc regime, see Figs. 3(a)–3(d) for the corresponding low-temperature results. Raising the temperature leads to increased deviations from the semiclassical approximation, with a broad maximum in several error measures around $T \simeq 0.1$ K. (b) wc regime, see Figs. 3(e)–3(h). We obtain similar results as in the sc case, but the deviations from the semiclassical approximation now remain close to or even below the 1% level at all temperatures studied.

strongly suppressed at low temperatures, taking values below the 1% level at most temperatures. As temperature increases, the error measures grow and reach a broad maximum around $T \simeq 0.1$ K, where they typically become of order 1%. This increase is again driven by thermal excitations of the double dot. Nevertheless, even near $T \simeq 0.1$ K, the semiclassical approximation remains rather accurate. We thus conclude that semiclassical estimates can be used throughout the considered temperature range in the wc limit.

In summary, the results in Fig. 5 show that thermal effects have the strongest impact if temperature becomes comparable with the double-dot level splitting. (For the chosen parameters, this happens for $T \simeq 0.1$ K.) In this case, the thermal occupation of the excited double-dot state enhances the photon-qubit fluctuations and thereby causes significant deviations from the semiclassical estimates. By contrast, at much lower temperatures, the double dot remains predominantly in its ground state, limiting the impact of thermal excitations on MBQ parity readout. For the parameters considered here, experimentally accessible temperatures $T \simeq 10$ mK stay well within this low-temperature regime.

IV. CONCLUSIONS

In this paper, we have studied charge reflectometry and capacitive readout of the parity degree of freedom associated with a Majorana pair in a MBQ. The central quantity of interest in both readout schemes is the parity-dependent dynamical susceptibility $\chi_z(\omega)$. We found a general expression for this quantity, see Eq. (40), which covers the entire crossover from the resonant sc regime to the off-resonant wc regime. We have also critically reexamined previous results which were obtained from the Lindblad equation by making a semiclassical factorization assumption, see Eq. (16). To assess the accuracy of this approximation, we have compared the corresponding approximate results to exact reference results by studying three different error measures as function of the system parameters, focusing on parameter regimes of current interest. The reference results have been obtained either by a numerical solution for the ss of the full Lindblad equation (in the sc case) or from exact analytical expressions (in the wc case). We find that, in the wc regime, the semiclassical approximation provides a quantitatively accurate description for the cavity response, with errors staying below the 0.1% level in all parameter regimes considered in this work. In the sc regime, however, results obtained under the semiclassical approximation typically deviate from the corresponding exact values by a few percent. While such deviations are not expected to create major problems for parity readout experiments, they may play an important role if the contrast between both parity values is not pronounced. In such cases, one should resort to a numerical solution of the full Lindblad equation.

ACKNOWLEDGMENTS

We thank K. Flensberg for discussions. We acknowledge funding by the Deutsche Forschungsgemeinschaft under Projektnummer 277101999–TRR 183 (Project No. C01) and under Germany's Excellence Strategy—Cluster of Excellence Matter and Light for Quantum Computing EXC 2004/2–390534769.

DATA AVAILABILITY

The data that support the findings of this article are openly available [52].

[1] V. Mourik, K. Zuo, S. M. Frolov, S. R. Plissard, E. P. A. M. Bakkers, and L. P. Kouwenhoven, Signatures of Majorana fermions in hybrid superconductor-semiconductor nanowire devices, Science **336**, 1003 (2012).

[2] L. Fu and C. L. Kane, Superconducting proximity effect and Majorana fermions at the surface of a topological insulator, Phys. Rev. Lett. **100**, 096407 (2008).

[3] M. Z. Hasan and C. L. Kane, Topological insulators, Rev. Mod. Phys. **82**, 3045 (2010).

[4] R. M. Lutchyn, E. P. A. M. Bakkers, L. P. Kouwenhoven, P. Krogstrup, C. M. Marcus, and Y. Oreg, Majorana zero modes in superconductor–semiconductor heterostructures, Nat. Rev. Mater. **3**, 52 (2018).

[5] E. Prada, P. San-Jose, M. W. A. de Moor, A. Geresdi, E. J. H. Lee, J. Klinovaja, D. Loss, J. Nygård, R. Aguado, and L. P. Kouwenhoven, From Andreev to Majorana bound states in hybrid superconductor–semiconductor nanowires, Nat. Rev. Phys. **2**, 575 (2020).

[6] C. W. J. Beenakker, Search for non-Abelian Majorana braiding statistics in superconductors, SciPost Phys. Lect. Notes 15 (2020).

[7] K. Flensberg, F. von Oppen, and A. Stern, Engineered platforms for topological superconductivity and Majorana zero modes, Nat. Rev. Mater. **6**, 944 (2021).

[8] M. Aghaee, A. Akkala, Z. Alam, R. Ali, A. Alcaraz Ramirez, M. Andrzejczuk, A. E. Antipov, P. Aseev, M. Astafev, B. Bauer, *et al.* (Microsoft Quantum), InAs-Al hybrid devices passing the topological gap protocol, Phys. Rev. B **107**, 245423 (2023).

[9] Microsoft Azure Quantum, M. Aghaee, A. Alcaraz Ramirez, Z. Alam, R. Ali, M. Andrzejczuk, A. Antipov, M. Astafev, A. Barzegar, B. Bauer, J. Becker, *et al.*, Interferometric single-shot parity measurement in InAs–Al hybrid devices, Nature (London) **638**, 651 (2025).

[10] M. Aghaee, Z. Alam, R. Andersen, M. Andrzejczuk, A. Antipov, M. Astafev, L. Avilovas, A. Azizimanesh, E. Banek, B. Bauer, *et al.*, Distinct lifetimes for X and Z loop measurements in a Majorana tetron device, arXiv:2507.08795.

[11] M. Leijnse and K. Flensberg, Parity qubits and poor man's Majorana bound states in double quantum dots, Phys. Rev. B **86**, 134528 (2012).

[12] T. Dvir, G. Wang, N. van Loo, C.-X. Liu, G. P. Mazur, A. Bordin, S. L. D. ten Haaf, J.-Y. Wang, D. van Driel, F. Zatelli, *et al.*, Realization of a minimal Kitaev chain in coupled quantum dots, Nature (London) **614**, 445 (2023).

[13] S. L. D. ten Haaf, Q. Wang, A. M. Bozkurt, C.-X. Liu, I. Kulesh, P. Kim, D. Xiao, C. Thomas, M. J. Manfra, T. Dvir, *et al.*, A two-site Kitaev chain in a two-dimensional electron gas, Nature (London) **630**, 329 (2024).

[14] M. Nitsch, L. Maffi, V. V. Baran, R. Seoane Souto, J. Paaske, M. Leijnse, and M. Burrello, Poor man's Majorana tetron, PRX Quantum **6**, 030365 (2025).

[15] N. van Loo, F. Zatelli, G. O. Steffensen, B. Roovers, G. Wang, T. Van Caekenberghe, A. Bordin, D. van Driel, Y. Zhang, W. D. Huisman, *et al.*, Single-shot parity readout of a minimal Kitaev chain, Nature (London) **650**, 334 (2026).

[16] S. Plugge, A. Rasmussen, R. Egger, and K. Flensberg, Majorana box qubits, New J. Phys. **19**, 012001 (2017).

[17] T. Karzig, C. Knapp, R. M. Lutchyn, P. Bonderson, M. B. Hastings, C. Nayak, J. Alicea, K. Flensberg, S. Plugge, Y. Oreg, *et al.*, Scalable designs for quasiparticle-poisoning-protected topological quantum computation with Majorana zero modes, Phys. Rev. B **95**, 235305 (2017).

[18] B. Béri and N. R. Cooper, Topological Kondo effect with Majorana fermions, Phys. Rev. Lett. **109**, 156803 (2012).

[19] A. Altland and R. Egger, Multiterminal Coulomb-Majorana junction, Phys. Rev. Lett. **110**, 196401 (2013).

[20] B. Béri, Majorana-Klein hybridization in topological superconductor junctions, Phys. Rev. Lett. **110**, 216803 (2013).
[21] L. A. Landau, S. Plugge, E. Sela, A. Altland, S. M. Albrecht, and R. Egger, Towards realistic implementations of a Majorana surface code, Phys. Rev. Lett. **116**, 050501 (2016).
[22] S. Plugge, L. A. Landau, E. Sela, A. Altland, K. Flensberg, and R. Egger, Roadmap to Majorana surface codes, Phys. Rev. B **94**, 174514 (2016).
[23] D. Litinski, M. S. Kesselring, J. Eisert, and F. von Oppen, Combining topological hardware and topological software: Color-code quantum computing with topological superconductor networks, Phys. Rev. X **7**, 031048 (2017).
[24] D. Litinski and F. von Oppen, Quantum computing with Majorana fermion codes, Phys. Rev. B **97**, 205404 (2018).
[25] D. Aasen, M. Aghaee, Z. Alam, M. Andrzejczuk, A. Antipov, M. Astafev, L. Avilovas, A. Barzegar, B. Bauer, J. Becker, *et al.*, Blueprint for fault-tolerant quantum computation with topological qubit arrays, Phys. Rev. Res. **7**, 041002 (2025).
[26] D. Aasen, M. Hell, R. V. Mishmash, A. Higginbotham, J. Danon, M. Leijnse, T. S. Jespersen, J. A. Folk, C. M. Marcus, K. Flensberg, *et al.*, Milestones toward Majorana-based quantum computing, Phys. Rev. X **6**, 031016 (2016).
[27] T. Hyart, B. van Heck, I. C. Fulga, M. Burrello, A. R. Akhmerov, and C. W. J. Beenakker, Flux-controlled quantum computation with Majorana fermions, Phys. Rev. B **88**, 035121 (2013).
[28] S. Vijay, T. H. Hsieh, and L. Fu, Majorana fermion surface code for universal quantum computation, Phys. Rev. X **5**, 041038 (2015).
[29] C. Ohm and F. Hassler, Microwave readout of Majorana qubits, Phys. Rev. B **91**, 085406 (2015).
[30] K. Yavilberg, E. Ginossar, and E. Grosfeld, Fermion parity measurement and control in Majorana circuit quantum electrodynamics, Phys. Rev. B **92**, 075143 (2015).
[31] S. Vijay and L. Fu, Teleportation-based quantum information processing with Majorana zero modes, Phys. Rev. B **94**, 235446 (2016).
[32] T. B. Smith, M. C. Cassidy, D. J. Reilly, S. D. Bartlett, and A. L. Grimsmo, Dispersive readout of Majorana qubits, PRX Quantum **1**, 020313 (2020).
[33] K. Gharavi, D. Hoving, and J. Baugh, Readout of Majorana parity states using a quantum dot, Phys. Rev. B **94**, 155417 (2016).
[34] M. I. K. Munk, R. Egger, and K. Flensberg, Fidelity and visibility loss in Majorana qubits by entanglement with environmental modes, Phys. Rev. B **99**, 155419 (2019).
[35] M. I. K. Munk, J. Schulenborg, R. Egger, and K. Flensberg, Parity-to-charge conversion in Majorana qubit readout, Phys. Rev. Res. **2**, 033254 (2020).
[36] J. F. Steiner and F. von Oppen, Readout of Majorana qubits, Phys. Rev. Res. **2**, 033255 (2020).
[37] G. Széchenyi and A. Pályi, Parity-to-charge conversion for readout of topological Majorana qubits, Phys. Rev. B **101**, 235441 (2020).
[38] Z.-T. Zhang and D. E. Liu, Readout of Majorana bound states via Landau-Zener transition, Phys. Rev. B **103**, 195401 (2021).
[39] J. Schulenborg, M. Burrello, M. Leijnse, and K. Flensberg, Multilevel effects in quantum dot based parity-to-charge conversion of Majorana box qubits, Phys. Rev. B **103**, 245407 (2021).
[40] J. Schulenborg, S. Krøjer, M. Burrello, M. Leijnse, and K. Flensberg, Detecting Majorana modes by readout of poisoning-induced parity flips, Phys. Rev. B **107**, L121401 (2023).
[41] C.-X. Liu, H. Pan, F. Setiawan, M. Wimmer, and J. D. Sau, Fusion protocol for Majorana modes in coupled quantum dots, Phys. Rev. B **108**, 085437 (2023).
[42] J. D. Sau and S. Das Sarma, Capacitance-based fermion parity readout and predicted Rabi oscillations in a Majorana nanowire, Phys. Rev. B **111**, 224509 (2025).
[43] K. D. Petersson, C. G. Smith, D. Anderson, P. Atkinson, G. A. C. Jones, and D. A. Ritchie, Charge and spin state readout of a double quantum dot coupled to a resonator, Nano Lett. **10**, 2789 (2010).
[44] T. Frey, P. J. Leek, M. Beck, A. Blais, T. Ihn, K. Ensslin, and A. Wallraff, Dipole coupling of a double quantum dot to a microwave resonator, Phys. Rev. Lett. **108**, 046807 (2012).
[45] J. I. Colless, A. C. Mahoney, J. M. Hornibrook, A. C. Doherty, H. Lu, A. C. Gossard, and D. J. Reilly, Dispersive readout of a few-electron double quantum dot with fast rf gate sensors, Phys. Rev. Lett. **110**, 046805 (2013).
[46] Y.-Y. Liu, K. D. Petersson, J. Stehlik, J. M. Taylor, and J. R. Petta, Photon emission from a cavity-coupled double quantum dot, Phys. Rev. Lett. **113**, 036801 (2014).
[47] A. Blais, R.-S. Huang, A. Wallraff, S. M. Girvin, and R. J. Schoelkopf, Cavity quantum electrodynamics for superconducting electrical circuits: An architecture for quantum computation, Phys. Rev. A **69**, 062320 (2004).
[48] H.-P. Breuer and F. Petruccione, *The Theory of Open Quantum Systems* (Oxford University Press, Oxford, 2007).
[49] L. Peri, M. Benito, C. J. B. Ford, and M. F. Gonzalez-Zalba, Unified linear response theory of quantum electronic circuits, npj Quantum Inf. **10**, 114 (2024).
[50] A. A. Clerk, M. H. Devoret, S. M. Girvin, F. Marquardt, and R. J. Schoelkopf, Introduction to quantum noise, measurement, and amplification, Rev. Mod. Phys. **82**, 1155 (2010).
[51] H. Bruus and K. Flensberg, *Many-Body Quantum Theory in Condensed Matter Physics—An Introduction* (Oxford University Press, Oxford, 2004).
[52] S. M. Benjadi and R. Egger, Parity readout in Majorana box qubits from the dispersive to the resonant regime [data set], Zenodo, 2026, https://doi.org/10.5281/zenodo.20623730.